Pentose Sugars Encode Sequence-Dependent DNA-RNA Segregation for Biomimetic Multiphase Condensates

Wei Guo[1,2,11,*], Feipeng Chen[1,11], Andrew B. Kinghorn[3,11], Xiufeng Li[2,4,11], Yi Pan[1,5], Rong Luo[2], Yuchao Wang[1], Kwan Kiu Lau[1], Tianjiao Mao[1], Fang Wang[1], Zhenyu Yang[1], Xiaolai Li[2], Ying Chen[6], Sihan Liu[1], Yage Zhang[7], Yang Song[8,*], Xiangze Zeng[9,*], Ho Cheung Shum[1,2,10,*]

1. Department of Mechanical Engineering, Faculty of Engineering, The University of Hong Kong, Hong Kong (SAR), Hong Kong, China.
2. Advanced Biomedical Instrumentation Centre, Hong Kong Science Park, Shatin, New Territories, Hong Kong (SAR), Hong Kong, China.
3. School of Biomedical Sciences, LKS Faculty of Medicine, The University of Hong Kong, Hong Kong (SAR), Hong Kong, China.
4. College of Food Science and Technology, Nanjing Agricultural University, Nanjing, 210095, Jiangsu, China.
5. Institute of Biomedical Engineering, College of Medicine, Southwest Jiaotong University, Chengdu, 610031, P.R.China.
6. Department of Ophthalmology, LKS Faculty of Medicine, The University of Hong Kong, Hong Kong (SAR), Hong Kong, China.
7. Guangdong Key Laboratory of Biomedical Measurements and Ultrasound Imaging, School of Biomedical Engineering, Shenzhen University Medical School, Shenzhen University, Shenzhen 518060, China.
8. State Key Laboratory of Metal Matrix Composites, School of Material Science and Engineering, Shanghai Jiao Tong University, Shanghai 200240, China.
9. Department of Physics, Hong Kong Baptist University, Kowloon Tong, Hong Kong, China.
10. Department of Chemistry and Department of Biomedical Engineering, City University of Hong Kong, Hong Kong SAR, China
11. These authors contribute equally to this work.

*Email: weiguo01@hku.hk; nanosurface@sjtu.edu.cn; xiangzezeng@hkbu.edu.hk; ashum@cityu.edu.hk

Abstract

DNA and RNA are compartmentalized into distinct, heterogeneous structures within cells. However, the separation between RNA and DNA, especially in the absence of modern transcription machinery, is inherently hindered by thermodynamic constraints such as complementary base pairing and entropic mixing. Here, we demonstrate that a single atomic difference in the pentose sugars of single-stranded DNA and RNA with identical sequences profoundly alters their interactions with cationic peptides, driving DNA-RNA segregation to form multiphase condensates. We reveal that the interplay between homotypic and heterotypic interactions among DNA, RNA and peptides dictates the formation of multiphase condensates. Leveraging this mechanism, we design a library of sequence-specific oligonucleotides, termed SEGREGamers, that enable programmable multiphase droplets with coexisting DNA-rich and RNA-rich domains. These synthetic condensates recapitulate key features of cellular nuclear compartments, including selective partitioning of small molecules, promotion of RNA aptamer folding, and enhancement of catalytic RNA cleavage. Our findings highlight the pivotal role of pentose sugar variations in nucleic acid compartmentalization, offering new insights into the evolutionary origins of nuclear organization and providing a versatile platform for engineering synthetic nuclear mimics, programmable molecular condensates, and RNA delivery vehicles.

Introduction

In the cell nucleus, DNA and RNA self-organize into distinct compartments for demarcation of separate nucleic functions[1, 2]. Chromatin, rich in DNA, serves as a stable archive for genetic information[3], while RNA-enriched structures, such as transcriptional condensates[2, 4] and nucleolus[5, 6], orchestrate DNA transcription and RNA processing required for protein synthesis. Despite the well-established genetic central dogma and transcriptional machinery[7], current understanding does not fully elucidate the efficient segregation of RNA and DNA, a process that occurs routinely yet remains thermodynamically counterintuitive. Specifically, the complementary base pairing between DNA and RNA is an enthalpically favorable exothermic process[8] and tends to be more stable than DNA-DNA hybrids[9]. Additionally, due to their homologous molecular structures[10], DNA and RNA tend to mix together for entropy increase[11]. These contradictions suggest an undiscovered mechanism to counteract the thermodynamic constraints and enable self-sorting of RNA and DNA into distinct compartments, especially when considering the primordial conditions before the emergence of modern cellular machinery[12].

Recent studies of nucleic acid and protein condensates have illuminated the complex architectures of DNA-rich chromatin[13, 14] and RNA-laden nuclear bodies[5, 6]. In particular, the burgeoning field of synthetic biology has recapitulated the dynamic phase behaviors of biological condensates[15-19], laying the groundwork for the artificial reconstruction of nuclear components and synthetic protocells[20-23]. The thermodynamic inclination toward multiphase droplet formation in polymolecular systems arises from an enthalpy-driven incompatibility that outweighs the entropy gain from mixing[24], suggesting that molecular complexity—rooted in sequence heterogeneity[25, 26], competitive intermolecular interactions[27-29], and kinetic arrests[30-32]—is cardinal to the genesis of such multiphase droplets. These droplets can assemble into superstructures that boast complex compositions or respond to external stimuli[33, 34], mirroring the complexity and responsivity of living systems. Nevertheless, there remains an unresolved scientific enigma: to what degree can molecular complexity be streamlined while still achieving multiphase separation in droplet assembly?

In this work, we demonstrate an unexpected molecular mechanism by which a minimal atomic distinction between single-stranded DNA (ssDNA) and RNA (ssRNA) oligonucleotides initiate their spatial segregation upon complexation with identical peptides. Intriguingly, the mere presence of a hydroxyl group (-OH) on the ribose 2' carbon of RNA, as opposed to a hydrogen atom (-H) on the DNA leads to disparate interaction during complex coacervation with cationic peptides. These differences are further modulated by specific sequence features that enhance DNA–DNA homotypic interactions, ultimately leading to the segregation of DNA and RNA into core–shell structured droplet phases. We have identified a collection of oligonucleotide motifs for ssDNA and ssRNA with identical sequences, called SEGREGamers, that can encode the segregation of DNA and RNA. This segregation can be programmed by the sequences and lengths of oligonucleotides, thereby facilitating the construction of

a multiphase droplet library with tunable phase-transition temperatures. This genetically encoded multiphase (GEM) droplet formulation can emulate the diverse functions of nuclear condensates, including partitioning of small molecules, RNA processing activities, and the modulation of ribozyme catalysis. Our results highlight the nuanced chemical dissimilarities between DNA and RNA, which could have shaped the evolution of protein-nucleic acid interactions in contemporary cellular machinery[35] and the spatial segregation of DNA-RNA in ancient cellular structures[36].

Results and Discussion

Multiphase droplets can be formed by sequence-identical ssDNA and ssRNA oligonucleotides.

Nuclear transcriptional condensates enrich both DNA and RNA, recruiting proteins for biogenesis[2, 4] (**Fig. 1A**). In addition, some DNA-binding transcription factors have been reported to exhibit affinity for RNA[37], while certain RNA-binding proteins can also interact with DNA counterparts[38, 39]. These observations suggest the presence of competitive DNA- and RNA-protein interactions (**Fig. 1B** and **Supplementary Fig. 1**), even when DNA and RNA have identical sequences (**Fig. 1C**). To explore whether these cooperative interactions could facilitate DNA-RNA segregation, we employed DNA and RNA oligonucleotides in combination with poly-L-lysine (PLL) as model systems. We selected the RNA oligonucleotide $[UUAGAA]_4$ (TERRA_M2), derived from the telomeric repeat-containing RNA (TERRA, $[UUAGGG]_n$), which contributes to telomeric heterochromatin formation. The two successive G-to-A mutations inhibit non-canonical G-quadruplex structures and promote droplet formation when complexed with PLL[40]. An intriguing observation emerged when studying oligonucleotide-PLL complex coacervation. Both $[UUAGAA]_4$ and its DNA counterpart, $[TTAGAA]_4$, formed droplets with PLL (**Fig. 1D**). Remarkably, when mixing $[UUAGAA]_4$, $[TTAGAA]_4$, and PLL together, core-shell multiphase droplets formed, with DNA localizing to the shell and RNA enriched in the core (**Fig. 1D**).

Quantitative fluorescence-activated cell sorting (FACS) analysis revealed that both fluorescently-labelled DNA and RNA were sequestered into droplets (**Fig. 1E**). Within multiphase droplets, DNA and RNA separated, forming a DNA-rich phase and an RNA-rich phase (**Fig. 1F** and **Supplementary Fig. 2**, A and B), suggesting segregation between DNA and RNA within droplets. To verify that the multiphase droplets were in a thermodynamic equilibrium state rather than merely kinetic intermediates, we mixed preformed DNA/PLL droplets and RNA/PLL droplets. Similar multiphase core-shell droplets that feature a DNA-rich shell and RNA-rich core were observed (**Fig. 1G** and **Supplementary Fig. 2C**), suggesting limited miscibility between DNA-PLL droplets and RNA-PLL droplets[25]. Additionally, these core-shell structured droplets displayed liquid-like properties, demonstrated by their ability to wet a glass slide (**Fig. 1H** and **Supplementary Fig. 3A**) and fuse with one another (**Supplementary Fig. 3B**). The liquid-like properties of both shell and core phases were further confirmed by fluorescence recovery after photobleaching (FRAP) measurements (**Supplementary Fig. 3C**).

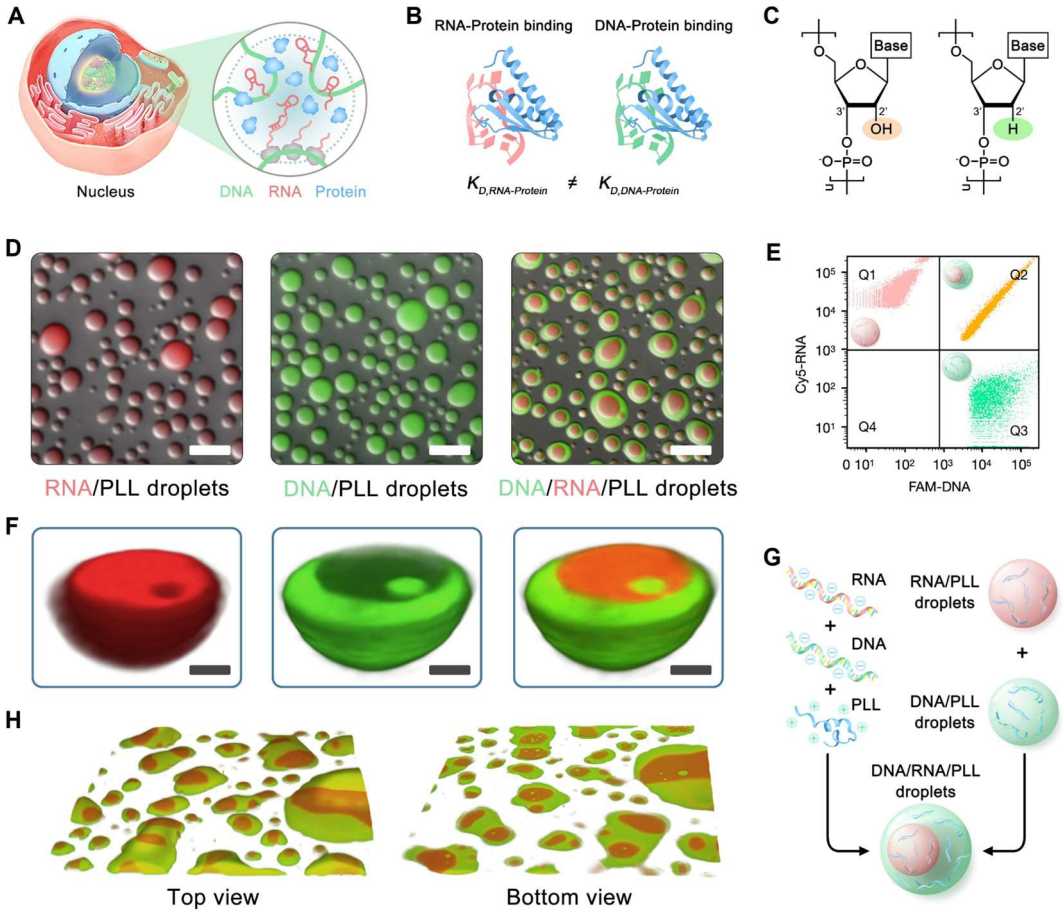

Fig. 1 | ssDNA and ssRNA oligonucleotides with the identical sequence form multiphase droplets. (**A**) Schematic of nuclear compartments within nucleus. (**B**) Competitive binding of proteins between DNA and RNA, where K is the association constant. (**C**) Molecular structure of RNA (red) and DNA (green). (**D**) Droplets formed by RNA-PLL, DNA-PLL and DNA-RNA-PLL phase separation. Droplets were prepared at the charge concentration of [e+] = [e-] = 5 mM in 500 mM KCl buffer. FAM-DNA and Cy5-RNA were used at 2 μM. For DNA-RNA-PLL phase separation, the [DNA] : [RNA] ratio was 1:1. Scale bar, 10 μm. (**E**) FACS fluorescence-gated analysis of the three types of droplets in (C). (**F**) Stacked confocal microscopy images of a multiphase DNA/RNA/PLL droplet. Scale bar, 2 μm. (**G**) Two equivalent pathways to form multiphase DNA/RNA/PLL droplets. (**H**) Glass wetting of multiphase DNA/RNA/PLL droplets. An observation box of 88.3 × 88.3 × 3.8 μm^3 is shown.

Distinct DNA- and RNA-PLL interaction strength results in multicomponent phase separation involving DNA-RNA segregation.

Interestingly, DNA-PLL complex coacervation formed solid-like aggregates at lower salt concentrations (100 and 300 mM KCl), while RNA-PLL complexation consistently produced liquid-like droplets (**Fig. 2A**). Gel-like aggregates can result from nucleic acid intra-/intermolecular hybridization[41, 42], increased charge density[41], and higher chain rigidity[43]. In our system, circular dichroism (CD) measurements indicated that DNA and RNA oligonucleotides do not form secondary structures on their own (**Supplementary Fig. 4**). Despite having identical sequences and similar charge densities, the formation of DNA/PLL aggregates and RNA/PLL droplets at lower salt

concentrations was attributed to distinct interactions with PLL. The enhanced hybridization propensity of DNA, as well as the possible formation of non-Watson–Crick structures, both aided by the electrostatic neutralization provided by PLL, may contribute to this aggregation[41]. Importantly, even at lower salt concentrations (100 and 300 mM KCl), mixing DNA, RNA, and PLL resulted in separate DNA-rich and RNA-rich domains within aggregates (**Supplementary Fig. 5**, A and B), although both domains exhibited a lower fluorescence recovery level in FRAP compared to multiphase droplets (**Supplementary Fig. 5C**). Consequently, increasing salt concentration via evaporation triggered the solid-to-liquid phase transition of multiphase aggregates (**Supplementary Fig. 5D** and **Supplementary Video 1**). Taken together, our data show that oligonucleotides $[UUAGAA]_4$ and $[TTAGAA]_4$, albeit with the identical sequence, confer phase immiscibility to DNA/RNA/PLL condensates at both liquid- and gel-like states.

To elucidate the mechanisms governing the formation of multiphase droplets, we characterized droplet rheology and interfacial tensions by colloidal probe atomic force microscopy[40, 44] (CP-AFM, **Fig. 2B**). The force-distance curves revealed that RNA/PLL droplets exhibit greater attraction forces compared to DNA/PLL droplets (**Fig. 2B** and **Supplementary Fig. 6**). Notably, the substantial difference in interfacial tension between DNA/PLL droplets ($\gamma_D \approx 0.89$ mN/m) and RNA/PLL droplets ($\gamma_R \approx 1.98$ mN/m) (**Fig. 2C** and supplementary text) points to the complete engulfment of RNA/PLL droplets by DNA/PLL droplets, which is crucial for the formation of core-shell structures[45] (**Fig. 2C**). Moreover, DNA/PLL droplets dissolved at 700 mM KCl, while RNA/PLL droplets remained stable even at 900 mM KCl (**Fig. 2A**). These data suggested that RNA-PLL interactions are stronger than those for DNA. Importantly, the stronger RNA-PLL interactions are also exhibited within multiphase droplets, as demonstrated by the higher salt resistance (**Supplementary Fig. 7A**) of the RNA-rich core phase, together with the more concentrated PLL distribution inside (**Supplementary Fig. 7B**).

The multiphase droplet formation indicates a three-phase coexistence region on the DNA-RNA-PLL phase diagram. To investigate how distinct RNA-PLL and DNA-PLL interaction strengths shape their phase diagram, we considered DNA- and RNA-PLL complexes at an equal charge ratio ([e+]:[e-] = 1:1). The competing effects of solvent-polymer complex and polymer complex-polymer complex interactions are summarized in **Fig. 2D**. Since interfacial tension is directly proportional to the Flory parameterχ[6, 46], it follows that $\chi_R > \chi_D$. Accordingly, a higher-dimensional multicomponent phase diagram was derived[47]. DNA-PLL complexes and RNA-PLL complexes condensed intoa polymer-rich phase under salt conditions where both DNA-PLL and RNA-PLL undergo phase separation (**Fig. 2E**). At a fixed salt concentration, the system has two-phase regions along the DNA and RNA axis, and a three-phase coexistence region in

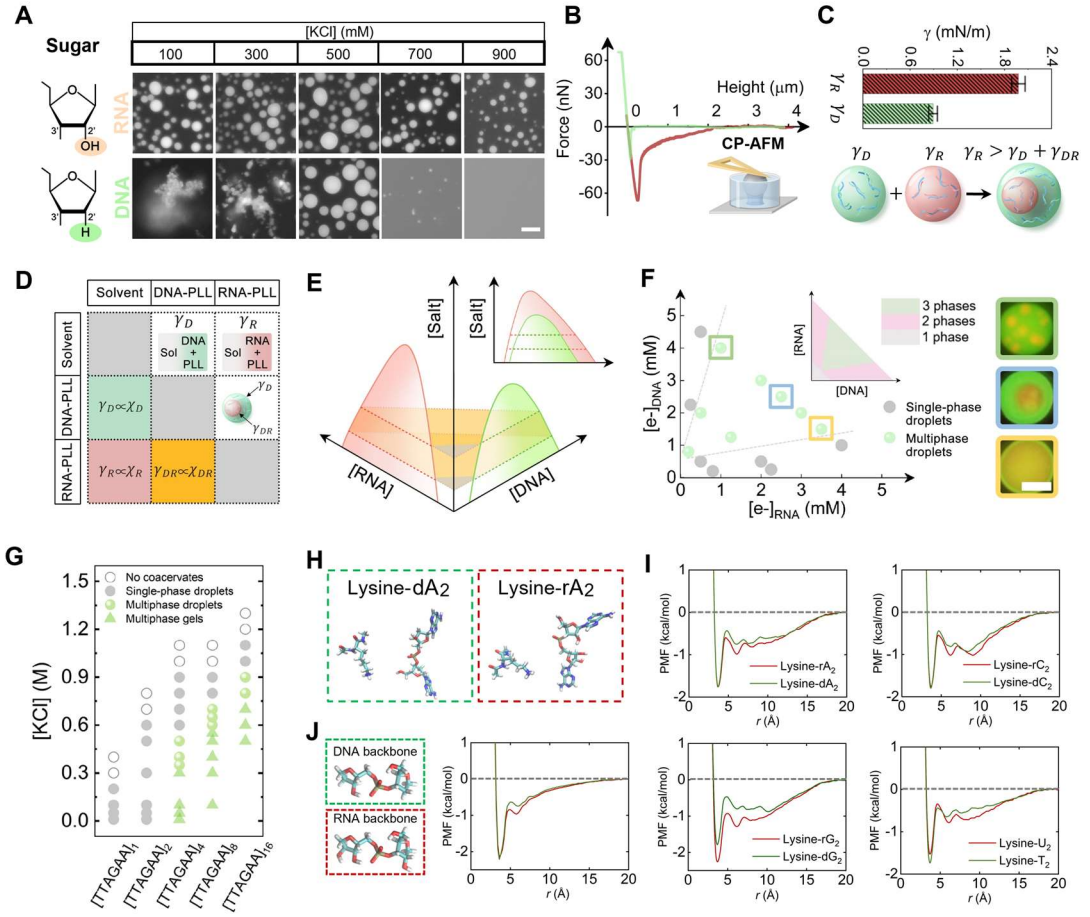

Fig. 2 | Pentose sugars encode distinct DNA-PLL and RNA-PLL interactions to drive multiphase droplet formation. (**A**) Fluorescent images of RNA- and DNA-PLL condensates at different KCl concentrations. Droplets were formed at the charge concentration of [e+] = [e-] = 5 mM. Scale bar, 10 μm. (**B**) Force-distance curves of DNA-PLL droplets (green) and RNA-PLL droplets (red) measured by colloidal probe atomic force microscopy (CP-AFM) for coacervate rheology measurement. (**C**) DNA-PLL droplets have lower interfacial tension than that of RNA-PLL droplets, enabling the engulfment of RNA droplets by DNA droplets. Error bars represent SEM (standard error of the mean) from five individual measurements. **D**) The interaction matrix for DNA/PLL, RNA/PLL, and DNA/RNA/PLL droplet formation. The positive correlation between interfacial tension γ and interaction strength χ indicates stronger interaction in RNA-PLL phase separation. (**E**) Three-dimensional phase diagram of DNA-PLL and RNA-PLL complex coacervation. Droplets containing both DNA and RNA formed at the light-yellow colored domain. Insert: Classical phase diagram of DNA- and RNA-PLL complex coacervation. (**F**) Phase diagram of DNA and RNA concentration-dependent multiphase droplet formation, with representative microscope images shown on the right. Scale bar, 5 μm. Insert: Phase diagram of PLL-scaffolded DNA-RNA segregation. (**G**) Chain length-dependent multiphase droplet formation across a range of salt concentrations. (**H**) All-atom molecular dynamics simulations of the interactions between lysine and dimerized deoxynucleotides or ribonucleotides. (**I**) Potential of mean force (PMF) profiles quantifying the interactions between lysine and each of the four (deoxy) nucleotide dimers. (**J**) All-atom simulations and corresponding PMF analyses of lysine interacting specifically with the sugar-phosphate backbones of deoxynucleotides and ribonucleotides. Unless otherwise noted, only DNA sequences are shown.

the middle[48] (Insert of **Fig. 2F**). To validate the phase diagram, we varied DNA and RNA concentrations while maintaining the charge ratio of 1:1. We observed that multiphase droplets formed when both DNA and RNA concentrations reached a critical value, while single-phase droplets formed if either concentration was below the critical value (**Fig. 2F**, **Supplementary Fig. 8**, A and B). The interface between the core and shell, along with the RNA/DNA stoichiometry-dependent core/shell size within multiphase droplets (**Fig. 2F**), suggest that DNA-PLL and RNA-PLL complexes exhibit segregative interactions, with $\chi_{DR} \propto \gamma_{DR}$. Such segregative interaction has been widely featured in all-aqueous two-phase systems (ATPS)[49]. Moreover, we found that, akin to ATPS, multiphase droplet formation is chain length dependent. Increasing the chain length of DNA and RNA enhanced segregative propensity between them, as indicated by the expanded salt concentration range for forming multiphase coacervates (**Fig. 2G**, **Supplementary Fig. 8C**). In contrast, no multiphase coacervates were observed for shorter-chain oligonucleotides, such as $[UUAGAA]_1$ and $[UUAGAA]_2$. Together, these results confirm that segregative interactions between DNA and RNA oligonucleotides drive multiphase droplet formation.

To test whether DNA-RNA segregation could be facilitated by other cationic polymers, we replaced PLL by other cationic polymers and found that Poly-D-lysine (PDL), Polydiallyldimethylammonium chloride (PDADMAC), Polyethyleneimine (PEI), and Poly-L-arginine (PLA) could also form multiphase droplets (**Supplementary Fig. 9A**). Notably, the salt conditions and DNA:RNA ratios varied for different cationic polymers due to the distinct charge densities and lengths of the individual polycations[27]. Additionally, we demonstrated that multiphase droplets formed when KCl was replaced by NaCl (**Supplementary Fig. 9B**). These findings suggest that DNA-RNA segregation is a universal phenomenon for complex coacervation and does not rely on specific polycation-dependent molecular interactions[27].

Differences in the sugar ring of oligonucleotides impact their interactions with PLL.

Distinct interactions of sequence-identical DNA and RNA with poly-L-lysine (PLL) are primarily attributed to differences in their sugar components. Specifically, DNA contains deoxyribose sugar, which lacks the 2'-OH group present in the ribose sugar of RNA. To further investigate the impact of sugar structures on the formation of nucleic acid-peptide condensates, we examined RNA oligonucleotides with 2'-O-methylation. These modified RNA oligonucleotides formed solid-like structures across a range of KCl concentrations from 100 to 700 mM (**Supplementary Fig. 10**). This observation indicates that sugar modifications significantly influence nucleic acid interactions with PLL and, consequently, the formation of condensates. Our findings are consistent with recent studies demonstrating that 2'-O-methylation alters percolation transition of RNA[50].

To explore the impact of the deoxyribose sugar in DNA and the 2'-OH group in the ribose sugar of RNA on their interactions with PLL at the atomistic level, we utilized

all-atom molecular dynamics simulations. We selected dimers of deoxyribonucleotides (e.g., dA2) and ribonucleotides (e.g., rA2) to represent DNA and RNA, respectively, and constructed a PLL monomer to interact with these nucleotide dimers (**Figure 2H**). Each ribonucleotide dimer contains two additional 2'-OH groups compared to each deoxyribonucleotide dimer (**Figure 2H**). Detailed simulation setups are described in the Materials and Methods section.

We assessed the potential of mean force (PMF) as a function of the intermolecular distance for different interacting sidechain pairs. Our results demonstrate that, for all four nucleobases, the PMF between lysine and ribonucleotide dimers is significantly stronger than that of deoxyribonucleotide dimers. This is consistent with experimental findings showing stronger RNA-PLL interactions compared to DNA-PLL interactions (**Figure 2I**). Notably, the differences in PMF between lysine-ribonucleotide and lysine-deoxyribonucleotide dimers are nucleobase-dependent, with the maximum difference observed for rG2/dG2 and the minimum for U2/T2 (**Figure 2I** and **Supplementary Figure 11**). These findings suggest that, in addition to electrostatic interactions between the NH^{3+} of lysine and the PO^{4-} of (deoxyribo)nucleotides, lysine-(deoxyribo)nucleotide dimer interactions are also mediated by nucleobases, potentially due to hydrogen bonds, cation-π, and π-π interactions. To further investigate the differences arising from sugars, we examined interactions between lysine and the DNA/RNA backbone, excluding nucleobases to isolate sugar effects (**Figure 2J**). Stronger interactions were confirmed between the RNA backbone and lysine compared to the DNA backbone, as indicated by a deeper PMF for lysine-RNA backbone interactions (**Figure 2J**). Overall, these simulation results confirm that the distinct RNA- and DNA-PLL interactions are fundamentally governed by differences in their sugar components.

Sequence-dependent assembly of DNA/RNA multiphase droplets.

Our all-atom molecular simulations demonstrated that nucleotide bases modulate interactions between nucleic acids and lysine residues, with guanine exhibiting the most substantial differences in interaction strength. These findings indicate that the DNA- and RNA-PLL interactions underlying multiphase condensate formation are sequence-dependent. To elucidate the molecular determinants underlying the sequence dependence of DNA/RNA multiphase condensate formation, we investigated the role of nucleic base patterning by generating three distinct variants of TERRA_M2 (TERRA_M2_Mut1, TERRA_M2_Mut2, and TERRA_M2_Mut3). Importantly, these sequences were designed to preserve the overall nucleotide composition of TERRA_M2 while eliminating potential secondary structures. Strikingly, two of the three DNA/RNA pairs were capable of forming multiphase condensates comparable to those formed by the native TERRA_M2 sequence (**Fig. 3A**), while TERRA_M2_Mut3 formed single-phase condensates. These results indicate that the specific sequence arrangement within TERRA_M2 plays a role in DNA-RNA segregation within condensates.

Then we explored other G-quadruplex-forming oligonucleotides with mutations similar to those in TERRA_M2, including PU22_M2, MT3_M2, TRF2_M2, NARS_M2, and hTERC_M2 (Supplementary Table 1). We observed multiphase droplets in PU22_M2, MT3_M2, and TRF2_M2 samples, whereas NARS_M2 and hTERC_M2 predominantly formed single-phase droplets (**Fig. 3B**). Notably, across all tested DNA/RNA oligonucleotides, RNA exhibited stronger interactions with PLL than DNA, reflected by higher critical salt concentrations required for droplet formation in both multiphase and single-phase systems (Supplementary Table 2). Sequence analysis revealed that TERRA_M2, PU22_M2, MT3_M2, and TRF2_M2 contained higher adenine content compared to NARS_M2 and hTERC_M2 (Supplementary Table 1). Moreover, complex coacervation of PLL with homo-oligonucleotides of dA_n/rA_n (n=22, 40) yielded inhomogeneous droplets, a phenomenon absent for T_n/U_n sequences (n=22, 40) (**Fig. 3C**, **Supplementary Fig. 12A**). In addition, N-to-A substitutions of TERRA_M2 and PU22_M2 at non-guanine sites formed multiphase droplets, while N-to-T/U substitutions did not (**Supplementary Fig. 12B**).

These results suggest that DNA-RNA segregation within condensates is promoted by adenine and suppressed by thymine/uracil. To test whether higher adenine content specifically enhances multiphase formation, we designed ten synthetic sequences with varying adenine fractions (Seq 1 highest A fraction, Seq 10 lowest; Supplementary Table 3). Surprisingly, only Seq 5 formed multiphase droplets (**Fig. 3D**, **Supplementary Fig. 13**), indicating that sequence-specific features beyond mere adenine content influence phase behavior. Next, we examined sequences with triplet repeats $[NNN]_8$, where two of the three nucleotides were fixed as adenine (A) to promote phase separation. Among the nine tested pairs, only $[AAG]_8$ and $[AGA]_8$ formed well-defined core-shell multiphase droplets, whereas $[GAA]_8$ formed gel-like, immiscible DNA- and RNA-rich domains (**Fig. 3E**). The remaining six sequences failed to produce multiphase condensates. These observations suggest that the presence of guanine within sequences containing high adenine content is critical for multiphase assembly, consistent with our atomistic findings that guanine encodes the strongest differences in DNA- and RNA-PLL interactions (**Fig. 2I**, **Supplementary Fig. S11**).

These results confirm that although an increased adenine fraction is correlated with a higher propensity for multiphase condensate formation, it is not a definitive predictor. To further dissect the contributions of sequence composition, we systematically analyzed additional parameters, including the fractions of cytosine (C), guanine (G), and pyrimidines (U and T). However, none of these compositional metrics established a clear threshold that could reliably distinguish sequences capable of forming multiphase condensates from those that cannot (**Supplementary Fig. S14**). Collectively, these findings indicate that the ability of DNA/RNA oligonucleotides to drive multiphase condensate formation cannot be fully explained by overall sequence content alone. This suggests that other aspects of sequence information—such as the presence of specific short sequence motifs or local sequence patterns—may play a critical role.

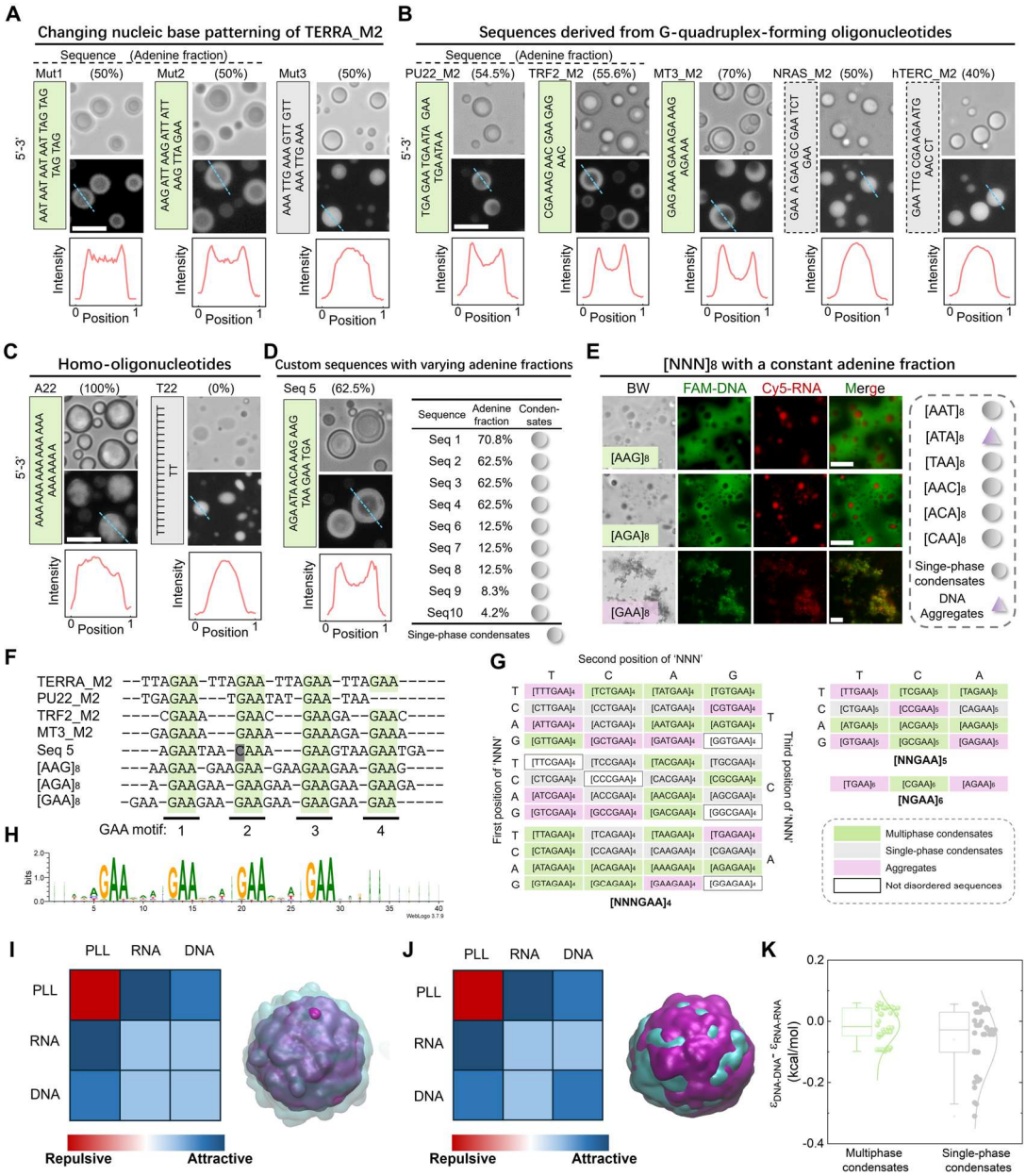

Fig. 3 | Sequence-dependent propensity of oligonucleotides for DNA/RNA/PLL multiphase condensate formation. (**A**) Varying nucleic base patterning of TERRA_M2 modulated multiphase condensate formation. Scale bar, 10 μm. (**B**) Motifs of PU22_M2, TRF2_M2 and MT3_M2 formed multiphase DNA/RNA/PLL droplets while motifs of NARS_M2 and hTERC_M2 did not. Scale bar, 10 μm. (**C**) Homo-oligonucleotides of A_{22} formed multi-phase condensates while T_{22} (U_{22}) formed single-phase condensates. Scale bar, 10 μm. (**D**) A custom designed motif Seq 5, formed multiphase droplets. Scale bar, 10 μm. **(E)** For disordered trinucleotide expansions that contain two adenines in each repeating units, only those contain guanines formed DNA/RNA/PLL multiphase condensates. (**F**) Colour-coded alignment of sequences capable of forming multiphase condensates revealed the recurrent presence of multiple 'GAA' motifs. (**G**) GAA-rich oligonucleotides with repeating units $[NNNGAA]_4$, $[NNGAA]_5$ and $[NGAA]_6$ exhibited sequence-dependent propensity for forming DNA/RNA/PLL multiphase condensates. (**H**) A consensus sequence motif was identified among all tested oligonucleotides that promote multiphase condensate formation. (**I**) Coarsen grained simulation of DNA/RNA/PLL multiphase

condensate formation via the comparable DNA-DNA and RNA-RNA interactions. (**J**) Single-phase droplets were formed when DNA-DNA interaction strength exceeds that of RNA-RNA interaction. (**K**) Oligonucleotides capable of forming multiphase condensates exhibited comparable RNA-RNA and DNA–DNA interactions compared to those forming single-phase condensates. Unless otherwise noted, only DNA sequences are shown.

'GAA'-rich sequences exhibit a strong propensity to drive the formation of multiphase condensates.

Sequence alignment of these eight multiphase-forming oligonucleotides—including TERRA_M2, PU22_M2, MT3_M2, TRF2_M2, Seq 5, $[AAG]_8$, $[AGA]_8$, and $[GAA]_8$—revealed they all contain multiple 'GAA' motifs (**Fig. 3F**), implicating these motifs in facilitating phase separation. Supporting this, a mutant with 'GGA' motifs (PU22_M1) failed to form multiphase droplets despite a higher guanine content (**Supplementary Fig. 15**). To further validate this hypothesis, we tested sequences associated with repeat expansion disorders, including $[NNNGAA]_4$, $[NGAA]_6$, and $[NNGAA]_5$, where N is any nucleotide (A, C, G, T/U). To minimize confounding effects of secondary structure, we excluded sequences predicted to form stable G-quadruplexes or i-motifs. Among 58 sequences tested, 26 formed core-shell condensates with RNA-rich cores and DNA-rich shells, 16 formed solid-like aggregates, and 16 remained as single-phase condensates (**Fig. 3G** and **Supplementary Fig. S16**). These findings reinforce that 'GAA'-rich sequences possess an intrinsic propensity to generate multiphase condensates with segregated DNA and RNA domains.

Sequence alignment and comprehensive analysis of all tested oligonucleotides revealed a strong correlation between the presence of 'GAA' motifs and multiphase condensate formation (**Fig. 3H**). Oligonucleotides capable of forming multiphase condensates consistently display a higher fraction of 'GAA' content, with an enrichment of guanine residues, compared to those that do not (Supplementary Table 3, **Supplementary Fig. S17**). Notably, these sequences also feature A-rich segments—serving as spacers—between 'GAA' motifs, in contrast to the more variable, non-A-rich gaps found in non-multiphase-forming sequences (**Supplementary Fig. S17**). These sequence-dependent properties of oligonucleotides capable of forming multiphase condensates suggest that multiphase condensate formation is governed by specific sequence-mediated interactions.

In ternary systems comprising DNA, RNA, and PLL, the emergence of multiphase condensates can be attributed to a finely tuned balance between heterotypic interactions and homotypic interactions[51]. This interplay highlights the importance of both the sequence composition of nucleic acids and the nature of their interactions with polycations in determining the architecture of the resulting condensates. In particular, we noticed that dA_n/rA_n sequence form the multiphasic droplet, whereas T_n/U_n sequence form the single-phase droplet. To probe these interactions, we employed the lattice based "sticker-and-spacer" model, and modelled poly-L-lysine, RNA, and DNA as linear chains of 20 stickers with isotropic potentials. Homotypic PLL interactions

were set to 0.1 k_BT, reflecting electrostatic repulsion. Heterotypic PLL-RNA and PLL-DNA interactions were assigned -0.28 k_BT and -0.2 k_BT, respectively. When RNA-RNA interactions were set to zero, core-shell droplets formed only when DNA-DNA interactions were comparable to RNA-RNA interactions. Increasing DNA-DNA interactions to -0.1 k_BT resulted in uniform, single-phase droplets (**Fig. 3I** and **J**), suggesting that enhanced DNA-DNA interactions relative to RNA-RNA interactions facilitate single-phase assembly formation. This conclusion is supported by comparative analyses indicating that sequences forming multiphase condensates display similar strengths of DNA–DNA and RNA–RNA interactions. In contrast, sequences that give rise to single-phase condensates exhibit stronger DNA–DNA interactions relative to RNA–RNA interactions (**Fig. 3K**). Previous studies have reported that stacking free energy for dA-dA and rA-rA, as well as for dG-dG and rG-rG, are nearly identical, whereas the stacking free energy of dT-dT exceeds that of rU-rU[52]. These differences likely underpin the preferential formation of G/A-rich oligonucleotides into multiphase structures, driven by a nuanced balance of homotypic and heterotypic interactions.

Notably,while recent studies suggest that single-chain rigidity of DNA and RNA can influence phase behavior[50, 53], experimental measurements indicate that the persistence lengths of ssDNA and ssRNA homopolymers-such as dT_{19}, rU_{19}, dA_{19}, and rA_{19}-are all similar, approximately 1 nm[54]. Consistently, our simulations show that ssDNA and ssRNA possess comparable chain flexibility, as reflected by their similar radius of gyration (R_g) distributions in the absence of PLL (**Supplementary Fig. S18**). However, conformational differences may emerge upon complexation with PLL[55], and the specific impact of sequence-dependent rigidity on complex coacervation remains unresolved. Collectively, our data indicates that the formation of multiphase versus single-phase condensates is primarily governed by the balance between homotypic and heterotypic interactions, while the contribution of single-chain rigidity to this process warrants further investigation.

Designer SEGREGamers enable programmable multiphase droplet formation and properties.

By integrating experimental observations with atomistic and coarse-grained simulations, we demonstrate that the formation of multiphase condensates by single-stranded DNA and RNA of identical sequence is fundamentally governed by structural differences at the 2′ position of their pentose sugars. Specifically, the presence of a 2′-hydroxyl group in RNA, as opposed to a 2′-hydrogen in DNA, results in stronger RNA-PLL interactions compared to DNA-PLL interactions. Furthermore, the emergence of multiphase, core-shell condensates is driven by a finely tuned balance between heterotypic (RNA-PLL, DNA-PLL) and homotypic (RNA-RNA, DNA-DNA) interactions in a sequence-dependent manner. Our data reveal that oligonucleotides containing multiple ‘GAA’ motifs interspersed with adenine-rich spacers exhibit a pronounced tendency to form multiphase condensates, characterized by the spatial segregation of DNA and RNA within a single droplet (**Fig. 4A**). On this basis, we define

'SEGREGamers' as DNA/RNA oligonucleotide pairs composed of multiple GAA motifs separated by adenine-rich linkers.

To assess whether this SEGREGamer motif can be systematically leveraged for the rational design of multiphase-forming oligonucleotides, we first investigated the behavior of a simple (GAA) repeat. As $[GAA]_8$ readily formed solid-like aggregates (**Fig. 3D**), we subsequently examined $[GAA]_7$ and three additional variants with single adenine insertions as spacers within the repeats. Strikingly, all four oligonucleotides robustly formed core–shell structured condensates (**Fig. 4B**), supporting the generalizability of the SEGREGamer design principle.

To further evaluate whether SEGREGamer motifs can be used as a generalizable platform for the *de novo* design of multiphase-forming oligonucleotides, we synthesized six distinct SEGREGamer sequences, each containing at least three GAA motifs. Of these, the four sequences with a higher number of adenine-rich gaps robustly formed multiphase condensates, whereas the two with fewer such gaps formed only single-phase droplets (**Figure 4C**, Supplementary Table 4). These results highlight the critical role of adenine-rich spacers in promoting multiphase behavior and underscore the SEGREGamer motif as a robust design principle for engineering DNA/RNA oligonucleotides with programmable phase properties.

To further test the modularity of this approach, we selected two wild-type sequences-NARS_M2 and hTERC_M2-that do not naturally form multiphase condensates. Upon engineering SEGREGamer-based variants by introducing two additional adenine residues at targeted gap positions, both modified sequences exhibited robust multiphase condensate formation (**Figure 4D**, **Supplementary Figure 19**). Collectively, these findings establish SEGREGamers as a versatile and modular motif for the rational design of DNA/RNA oligonucleotides with enhanced propensity for multiphase condensate formation.

Given the high degree of sequence programmability inherent to both DNA and RNA, we next investigated whether this property extends to the programmable control of multiphase droplet architectures. To this end, we designed diblock DNA and RNA oligonucleotides comprising distinct sequence modules. For a broader perspective, we selected the T7 promoter as one block (S1), and TERRA_M2 (S2) and PU22_M2 (S3) as additional blocks (**Figure 4E** and Supplementary Table 5). As shown in **Figure 4F**, diblock constructs such as d(S1-b-S2) and d(S1-b-S3) readily formed multiphase droplets with their corresponding RNA partners (rS2 and rS3), despite S1 alone being unable to induce multiphase formation (**Supplementary Figure 20**). Similarly, diblock DNA and RNA oligonucleotides based on d(S2-b-S3) and r(S2-b-S3) also supported multiphase droplet formation. These results confirm that the sequence-encoded information driving multiphase condensate formation can be modularly incorporated into larger, genetically programmable nucleic acid constructs, offering a generalizable strategy for engineering complex biomolecular condensates.

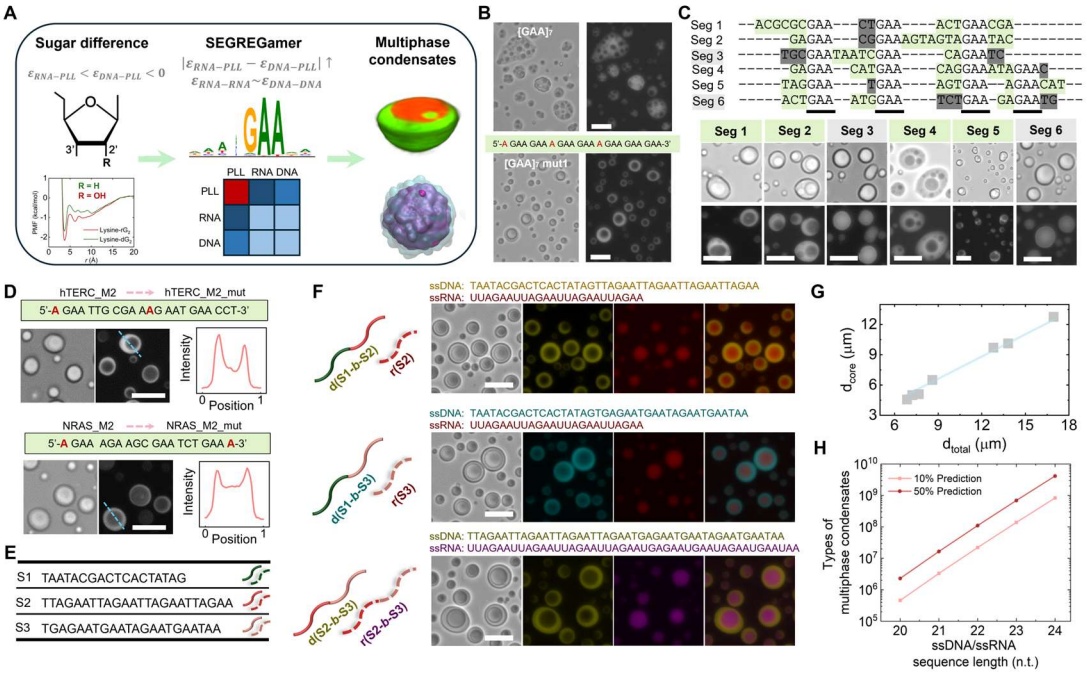

Fig. 4 | Designer SEGREGamers of DNA and RNA oligonucleotides for formulating programmable multiphase droplets. (**A**) Mechanism underlying multiphase condensate formation. Pentose sugars give rise to distinct DNA– and RNA–PLL interactions, which are further modulated by specific sequences containing GAA-rich motifs and A-rich gaps. These features promote enhanced DNA–DNA homotypic interactions, driving the assembly of multiphase condensates. (**B**) $[GAA]_7$ formed multiphase condensates, while its mutant containing three adenine insertions generated well-defined core–shell structured multiphase droplets. Scale bar, 10 μm. (**C**) Custom-designed SEGREGamers, featuring varying numbers of 'GAA' repeats interspersed with adenine-containing linker regions (highlighted in green) exhibited a strong propensity to form multiphase condensates. Scale bar, 10 μm. (**D**) SEGREGamer-guided rationally designed NARS_M2 and hTERC_M2 mutants formed multiphase droplets. Scale bar, 10 μm. (**E**) Motifs used as diblock units. (**F**) Multiphase droplets formed by diblock ssDNA and ssRNA. Fluorescence channels of diblock ssDNA and ssRNA were false colored for enhanced contrast. Scale bar, 10 μm. (**G**) Correlation between the core and the total size of multiphase droplets. (**H**) The diversity of multiphase condensates formed by the SEGREGamer library as a function of sequence length. Unless otherwise noted, only DNA sequences are shown.

To further investigate multiphase droplet properties under controlled conditions, we employed a droplet microfluidic platform designed for forming highly uniform core-shell structured coacervate droplets (**Supplementary Fig. 21A** and **B**). By varying the volume of water-in-oil microdroplets, we found that the multiphase droplet size increases with the number of biomolecules participating in the phase separation. A self-similarity relationship was observed between water-in-oil droplet size, multiphase droplet size (d_{total}), and core size (d_{core}), along with a scaling law of $d_{core} \sim d_{total}$ (**Supplementary Fig. 21C**, **Fig. 4G**). Given the superior programmability and tunability of SEGREGamers, we next sought to estimate the potential diversity of multiphase condensates achievable using this design strategy. Our combinatorial analysis indicates that, even under a conservative assumption of a 10% success rate, it

is possible to generate a library of approximately 10^5 distinct multiphase condensate types using 20-mer SEGREGamer sequences, and up to 10^9 types with 24-mer sequences (**Figure 4H**, Supplementary Text). Notably, this diversity is expected to increase substantially as prediction accuracy and success rates improve.

Multiphase droplets as model systems to mimic nuclear condensates.

For a proof-of-concept application, we elucidated the potential of multiphase droplets as synthetic nuclear compartments with spatial and functional heterogeneity. Nuclear compartments play vital roles in intracellular compartmentalization, including the uptake of small molecule therapeutics[56], RNA biogenesis and processing, and catalytic reaction regulation (**Fig. 5A**). We first examined the partitioning of small fluorophore molecules with varying properties in multiphase droplets. As shown in **Fig. 5B**, DNA-staining molecules, DAPI and SYBR Green I, were enriched within the DNA-rich shell. In contrast, hydrophobic molecules like ThT concentrated within the RNA-rich core phase due to the higher polymer density (less water content) caused by stronger RNA-PLL interactions. Similarly, negatively charged dATP was enriched within the core phase with more PLL. We also tested other small molecules, including N-Methyl Mesoporphyrin IX (NMM), Nile Red, methylene blue, and Rhodamine B (**Supplementary Fig. 22**). Collectively, our findings indicate that all small fluorophore molecules are concentrated by multiphase droplets, but with varying spatial distributions. These results suggest multiphase droplets selectively partition small molecules based on the distinct microenvironments of DNA-rich shell and RNA-rich core.

We then looked at the capability of multiphase droplets as a model system for RNA biogenesis and processing using fluorophore-binding RNA aptamers. We chose the 49-nucleotide fluorescent RNA Broccoli aptamer, which activates DFHBI-1T's green fluorescence when folded[57] **(Fig. 5C**). To disentangle the distributions of the fluorophore-bound and unbound RNA aptamers, we used the red fluorescently labeled RNA aptamer sequence. The red fluorescence profile suggests equal distribution of total RNA aptamer molecules between shell and core regions. However, the green fluorescence demonstrated a higher intensity in the shell phase **(Fig. 5D** and **Supplementary Fig. 23A**), indicating fluorophore-bound RNA aptamers were enriched in the DNA-rich phase. The partitioning of RNA aptamer and DFHBI-1T individually within multiphase droplets suggests both entities are enriched in the core phase (**Supplementary Fig. 23**, B and C). We concluded that fluorophore binding and folding of the RNA aptamer alter its partitioning behaviors within multiphase droplets, with structured and bound RNA localizing to the shell phase. This RNA structure-partitioning interplay within multiphase droplets is reminiscent of rRNA processing in the nucleolus, where fully processed and folded RNA is excluded from the core to the shell phase due to decreased valence of folded RNA[5, 58]. The partitioning of G-quadruplex containing rPU22 and its mutant rPU22_M2 demonstrated similar thermodynamics, with rPU22 more likely to localize in the shell phase (**Supplementary Fig. 24**). Quantitatively, the Gibbs free energy of RNA partitioning

(**Fig. 5E**) is consistent with the equilibrium energetic landscape of ribosome RNA exclusion within the nucleolus, highlighting the capability of multiphase droplets as synthetic nuclear compartments with functional heterogeneity.

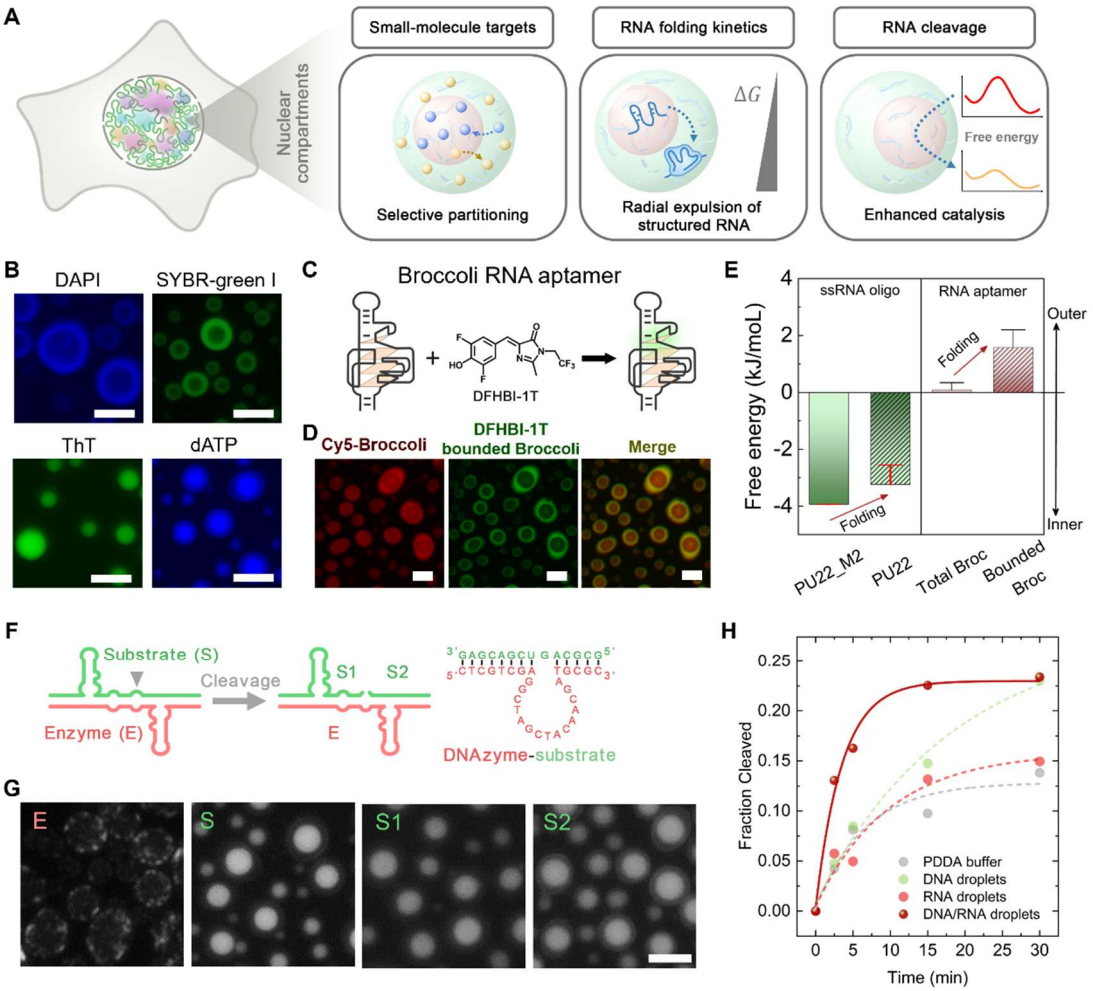

Fig. 5 | Mimicking of nuclear compartments using multiphase droplets. (**A**) Functions of nuclear compartments. (**B**) Selective partitioning of small molecules within the core and shell phase of multiphase droplets. (**C**) Broccoli RNA aptamer lights up the fluorophore molecule via folding and binding. (**D**) Distribution of the total Broccoli aptamer (red) and fluorophore-bound Broccoli aptamer (green) within multiphase droplets. (**E**) RNA structural folding altered their partitioning thermodynamics in a way from the core to shell phase. Error bars represent SEM from the analysis of thirty individual condensates. (**F**) RNA cleavage by a DNAzyme, with the cleavage site shown by the triangle. (**G**) Uptake of fluorescently labelled DNAzyme (E), RNA substrate (S), and cleaved RNA segments (S1 and S2) within multiphase DNA/RNA/PDDA droplets. Scale bar, 10 μm. (**H**) Enhanced RNA cleavage within multiphase droplets. The data points are derived from gel analysis. The curves are the best fit.

Finally, we explored the ability of multiphase droplets to regulate RNA cleavage reactions using the 10-23 DNAzyme cleavage reaction[59] (**Fig. 5F**). We found that the DNAzyme (E) was partitioned into the shell phase, while the RNA substrate (S) and resulting cleavage products (S1 and S2, **Supplementary Table 6**) enriched within the core phase (**Fig. 5G**). Interestingly, despite the distinct partitioning behaviors of

DNAzyme and RNA substrate within core-shell droplets, DNAzyme catalytic efficiency in multiphase droplets exhibited improvement compared to reactions in DNA or RNA droplets alone, particularly during the early reaction stage (**Fig. 5H** and **Supplementary Fig. 25**). The enhancement of this reaction can be attributed to two factors: 1) increased catalysis at the interface, which occurs due to higher local concentrations of both DNAzyme and RNA substrate near the boundary between the shell and core phases, and 2) the separation between DNAzyme and cleavage RNA products, which results in a further increase in catalytic efficiency. The latter occurs as the loss of RNA substrate from the reaction is compensated for, and the newly formed RNA products are transferred to the core phase, with both processes driven by the re-equilibrated RNA partitioning. Consequently, the catalytic reaction progresses towards completion in accordance with Le Chatelier's principle[60]. Our results demonstrate the potential of multiphase droplets as model nuclear compartments for RNA cleavage.

Conclusions

In summary, we have demonstrated a molecular mechanism that can be deployed to form a library of genetically encoded multiphase droplets. We found the unique sugar groups in ssDNA and ssRNA oligonucleotides, even for DNA and RNA with identical sequences, result in different interaction strengths with cationic peptides, with RNA being stronger than DNA. This difference promotes a sequence-dependent segregation between DNA and RNA oligonucleotides within complex coacervates, ultimately driving the formation of multiphase droplets featuring DNA-rich shell and RNA-rich core. Remarkably, these multiphase droplet-forming oligonucleotides, termed SEGREGamers, enable the programmed formation and biophysical properties of multiphase condensates at single-nucleotide resolution, allowing for the top-down design of condensates with desired properties for the mimicry of the heterogenous nuclear environment.

Interestingly, these GAA motifs in SEGREGamers that form multiphase droplets result in low sequence complexity, reminiscent of short tandem repeats (STRs) found in genomes, which are associated with gene expression and diseases, such as Friedreich's ataxia GAA repeats[61]. A recent study demonstrated that STRs can interact directly with various transcription factors (TFs), exhibiting a binding strength weaker than regulatory genomic sequences but stronger than random genomic sequences, thereby facilitating the localization of TFs to specific binding targets within genomes[35]. We hypothesize that a similar mechanism could exist for SEGREGamers, allowing for finely tuned DNA-peptide and RNA-peptide interaction strengths and subsequently facilitating DNA-RNA segregation within multiphase droplets. Meanwhile, such cationically scaffolded DNA-RNA segregation could be a phase transition mechanism *in vivo*, as evidenced by a recent discovery that different mRNA identities undergo protein-scaffolded demixing and form multiphase condensates to modulate translation[62].

Multiphase coacervate droplets, with their structural and functional heterogeneity, have

been suggested as synthetic compartments resembling intracellular membraneless organelles[16], potentially playing crucial roles in the origin of life[63]. Our research presents a robust synthetic pathway for multiphase droplets using basic DNA and RNA building blocks, without relying on complex competing biomolecular interaction networks. Thus, our multiphase droplet formulation represents a minimal model system of transcriptional condensates around the genome that share components but remain mutually immiscible[64]. These droplets can be integrated into existing protocell systems as synthetic nuclear compartments for cellular heterogeneity[20], and into the 'RNA-DNA world' hypothesis for early molecule catalysis and evolution[65, 66]. Furthermore, with potentials in achieving designer functions from designer sequences, the DNA/RNA-encoded immiscibility can be combined with DNA/RNA nanotechnology to enable precise RNA delivery[67], multiscale superstructure assembly[68], and DNA based hydrogels[69].

References

1. Rinn, J. & Guttman, M. RNA and dynamic nuclear organization. *Science* **345**, 1240-1241 (2014).
2. Sabari, B.R. et al. Coactivator condensation at super-enhancers links phase separation and gene control. *Science* **361**, eaar3958 (2018).
3. Kagey, M.H. et al. Mediator and cohesin connect gene expression and chromatin architecture. *Nature* **467**, 430-435 (2010).
4. Henninger, J.E. et al. RNA-Mediated Feedback Control of Transcriptional Condensates. *Cell* **184**, 207-225.e224 (2021).
5. Lafontaine, D.L.J., Riback, J.A., Bascetin, R. & Brangwynne, C.P. The nucleolus as a multiphase liquid condensate. *Nature Reviews Molecular Cell Biology* **22**, 165-182 (2021).
6. Feric, M. et al. Coexisting Liquid Phases Underlie Nucleolar Subcompartments. *Cell* **165**, 1686-1697 (2016).
7. Alberts, B. Molecular biology of the cell. (Garland science, 2017).
8. Nudler, E., Mustaev, A., Goldfarb, A. & Lukhtanov, E. The RNA-DNA Hybrid Maintains the Register of Transcription by Preventing Backtracking of RNA Polymerase. *Cell* **89**, 33-41 (1997).
9. Santos-Pereira, J.M. & Aguilera, A. R loops: new modulators of genome dynamics and function. *Nature Reviews Genetics* **16**, 583-597 (2015).
10. Yadav, M., Kumar, R. & Krishnamurthy, R. Chemistry of Abiotic Nucleotide Synthesis. *Chemical Reviews* **120**, 4766-4805 (2020).
11. Flory, P., Orwoll, R. & Vrij, A. Statistical thermodynamics of chain molecule liquids. I. An equation of state for normal paraffin hydrocarbons. *Journal of the American Chemical Society* **86**, 3507-3514 (1964).
12. Gavette, J., Stoop, M., Hud, N. & Krishnamurthy, R. RNA-DNA Chimeras in the Context of an RNA World Transition to an RNA/DNA World. *Angewandte Chemie (International ed. in English)* **55** (2016).
13. Gallego, L.D. et al. Phase separation directs ubiquitination of gene-body nucleosomes. *Nature* **579**, 592-597 (2020).
14. Shin, Y. et al. Liquid Nuclear Condensates Mechanically Sense and Restructure the Genome. *Cell* **175**, 1481-1491.e1413 (2018).
15. Choi, S., Meyer, M.O., Bevilacqua, P.C. & Keating, C.D. Phase-specific RNA accumulation and duplex thermodynamics in multiphase coacervate models for membraneless organelles. *Nature Chemistry* **14**, 1110-1117 (2022).
16. Yewdall, N.A., André, A.A.M., Lu, T. & Spruijt, E. Coacervates as models of membraneless organelles. *Current Opinion in Colloid & Interface Science* **52**, 101416 (2021).
17. Li, Q. et al. Synthetic Membraneless Droplets for Synaptic-Like Clustering of Lipid Vesicles. *Angewandte Chemie International Edition* **n/a**, e202313096 (2023).
18. Wadsworth, G.M. et al. RNAs undergo phase transitions with lower critical solution temperatures. *Nature Chemistry* **15**, 1693-1704 (2023).
19. Chen, W. et al. Ballistic diffusion fronts in biomolecular condensates. *Nature Nanotechnology* (2025).
20. Xu, C., Martin, N., Li, M. & Mann, S. Living material assembly of bacteriogenic protocells.

Nature **609**, 1029-1037 (2022).
21. Do, S., Lee, C., Lee, T., Kim, D.-N. & Shin, Y. Engineering DNA-based synthetic condensates with programmable material properties, compositions, and functionalities. *Science Advances* **8**, eabj1771 (2022).
22. Samanta, A., Sabatino, V., Ward, T.R. & Walther, A. Functional and morphological adaptation in DNA protocells via signal processing prompted by artificial metalloenzymes. *Nature Nanotechnology* **15**, 914-921 (2020).
23. Tran, M.P. et al. Genetic encoding and expression of RNA origami cytoskeletons in synthetic cells. *Nature Nanotechnology* **20**, 664-671 (2025).
24. Brangwynne, Clifford P., Tompa, P. & Pappu, Rohit V. Polymer physics of intracellular phase transitions. *Nature Physics* **11**, 899-904 (2015).
25. Lu, T. & Spruijt, E. Multiphase Complex Coacervate Droplets. *Journal of the American Chemical Society* **142**, 2905-2914 (2020).
26. Simon, J.R., Carroll, N.J., Rubinstein, M., Chilkoti, A. & López, G.P. Programming molecular self-assembly of intrinsically disordered proteins containing sequences of low complexity. *Nature Chemistry* **9**, 509-515 (2017).
27. Fisher, R.S. & Elbaum-Garfinkle, S. Tunable multiphase dynamics of arginine and lysine liquid condensates. *Nature Communications* **11**, 4628 (2020).
28. Boeynaems, S. et al. Spontaneous driving forces give rise to protein–RNA condensates with coexisting phases and complex material properties. *Proceedings of the National Academy of Sciences* **116**, 7889-7898 (2019).
29. Kaur, T. et al. Sequence-encoded and composition-dependent protein-RNA interactions control multiphasic condensate morphologies. *Nature Communications* **12**, 872 (2021).
30. Merindol, R., Loescher, S., Samanta, A. & Walther, A. Pathway-controlled formation of mesostructured all-DNA colloids and superstructures. *Nature Nanotechnology* **13**, 730-738 (2018).
31. Shen, Y. et al. The liquid-to-solid transition of FUS is promoted by the condensate surface. *Proceedings of the National Academy of Sciences* **120**, e2301366120 (2023).
32. Lin, A.Z. et al. Dynamical control enables the formation of demixed biomolecular condensates. *Nature Communications* **14**, 7678 (2023).
33. Mu, W. et al. Superstructural ordering in self-sorting coacervate-based protocell networks. *Nature Chemistry* (2023).
34. Liu, S. et al. Enzyme-mediated nitric oxide production in vasoactive erythrocyte membrane-enclosed coacervate protocells. *Nature Chemistry* **12**, 1165-1173 (2020).
35. Horton, C.A. et al. Short tandem repeats bind transcription factors to tune eukaryotic gene expression. *Science* **381**, eadd1250 (2023).
36. Blain, J.C. & Szostak, J.W. Progress Toward Synthetic Cells. *Annual Review of Biochemistry* **83**, 615-640 (2014).
37. Oksuz, O. et al. Transcription factors interact with RNA to regulate genes. *Molecular cell* **83**, 2449-2463.e2413 (2023).
38. Lingel, A., Simon, B., Izaurralde, E. & Sattler, M. Structure and nucleic-acid binding of the Drosophila Argonaute 2 PAZ domain. *Nature* **426**, 465-469 (2003).
39. Hudson, W.H. & Ortlund, E.A. The structure, function and evolution of proteins that bind DNA and RNA. *Nature Reviews Molecular Cell Biology* **15**, 749-760 (2014).

40. Guo, W. et al. Tuning Material States and Functionalities of G-Quadruplex-Modulated RNA-Peptide Condensates. *Journal of the American Chemical Society* **145**, 2375-2385 (2023).
41. Vieregg, J.R. et al. Oligonucleotide–Peptide Complexes: Phase Control by Hybridization. *Journal of the American Chemical Society* **140**, 1632-1638 (2018).
42. Jain, A. & Vale, R.D. RNA phase transitions in repeat expansion disorders. *Nature* **546**, 243-247 (2017).
43. Shakya, A. & King, J.T. DNA Local-Flexibility-Dependent Assembly of Phase-Separated Liquid Droplets. *Biophysical Journal* **115**, 1840-1847 (2018).
44. Li, X., van der Gucht, J., Erni, P. & de Vries, R. Active microrheology of protein condensates using colloidal probe-AFM. *Journal of Colloid and Interface Science* **632**, 357-366 (2023).
45. Gouveia, B. et al. Capillary forces generated by biomolecular condensates. *Nature* **609**, 255-264 (2022).
46. Mao, S., Chakraverti-Wuerthwein, M.S., Gaudio, H. & Ko š mrlj, A. Designing the Morphology of Separated Phases in Multicomponent Liquid Mixtures. *Physical Review Letters* **125**, 218003 (2020).
47. Chen, X., Chen, E.-Q., Shi, A.-C. & Yang, S. Multiphase Coacervates Driven by Electrostatic Correlations. *ACS Macro Letters* **10**, 1041-1047 (2021).
48. Shin, Y. & Brangwynne, C.P. Liquid phase condensation in cell physiology and disease. *Science* **357**, eaaf4382 (2017).
49. Chao, Y. & Shum, H.C. Emerging aqueous two-phase systems: from fundamentals of interfaces to biomedical applications. *Chemical Society Reviews* (2020).
50. Wadsworth, G.M., Aierken, D., Thurston, G.M., Joseph, J.A. & Banerjee, P.R. The Critical Role of the 2'-OH group in Phase Separation and Percolation Transitions of RNA. *bioRxiv : the preprint server for biology*, 2025.2002.2026.638501 (2025).
51. Farag, M., Borcherds, W.M., Bremer, A., Mittag, T. & Pappu, R.V. Phase separation of protein mixtures is driven by the interplay of homotypic and heterotypic interactions. *Nature Communications* **14**, 5527 (2023).
52. Brown, R.F., Andrews, C.T. & Elcock, A.H. Stacking Free Energies of All DNA and RNA Nucleoside Pairs and Dinucleoside-Monophosphates Computed Using Recently Revised AMBER Parameters and Compared with Experiment. *Journal of Chemical Theory and Computation* **11**, 2315-2328 (2015).
53. André, A.A.M. & Spruijt, E. Rigidity Rules in DNA Droplets: Nucleic Acid Flexibility Affects Model Membraneless Organelles. *Biophysical Journal* **115**, 1837-1839 (2018).
54. Nüesch, M.F. et al. Nanosecond chain dynamics of single-stranded nucleic acids. *Nature Communications* **15**, 6010 (2024).
55. Tian, F.-J. et al. Universality in RNA and DNA deformations induced by salt, temperature change, stretching force, and protein binding. *Proceedings of the National Academy of Sciences* **120**, e2218425120 (2023).
56. Klein, I.A. et al. Partitioning of cancer therapeutics in nuclear condensates. *Science* **368**, 1386-1392 (2020).
57. Filonov, G.S., Moon, J.D., Svensen, N. & Jaffrey, S.R. Broccoli: rapid selection of an RNA mimic of green fluorescent protein by fluorescence-based selection and directed evolution. *J Am Chem Soc* **136**, 16299-16308 (2014).

58. Riback, J.A. et al. Composition-dependent thermodynamics of intracellular phase separation. *Nature* **581**, 209-214 (2020).
59. Santoro, S.W. & Joyce, G.F. A general purpose RNA-cleaving DNA enzyme. *Proceedings of the National Academy of Sciences* **94**, 4262-4266 (1997).
60. Dewey, D.C., Strulson, C.A., Cacace, D.N., Bevilacqua, P.C. & Keating, C.D. Bioreactor droplets from liposome-stabilized all-aqueous emulsions. *Nature Communications* **5**, 4670 (2014).
61. Shishkin, A.A. et al. Large-Scale Expansions of Friedreich's Ataxia GAA Repeats in Yeast. *Molecular cell* **35**, 82-92 (2009).
62. Cardona, A.H. et al. Self-demixing of mRNA copies buffers mRNA:mRNA and mRNA:regulator stoichiometries. *Cell*.
63. Poudyal, R.R., Pir Cakmak, F., Keating, C.D. & Bevilacqua, P.C. Physical Principles and Extant Biology Reveal Roles for RNA-Containing Membraneless Compartments in Origins of Life Chemistry. *Biochemistry* **57**, 2509-2519 (2018).
64. Sabari, B.R., Dall'Agnese, A. & Young, R.A. Biomolecular Condensates in the Nucleus. *Trends in Biochemical Sciences* **45**, 961-977 (2020).
65. Xu, J. et al. Selective prebiotic formation of RNA pyrimidine and DNA purine nucleosides. *Nature* **582**, 60-66 (2020).
66. Leu, K., Obermayer, B., Rajamani, S., Gerland, U. & Chen, I.A. The prebiotic evolutionary advantage of transferring genetic information from RNA to DNA. *Nucleic Acids Research* **39**, 8135-8147 (2011).
67. Hu, Q., Li, H., Wang, L., Gu, H. & Fan, C. DNA Nanotechnology-Enabled Drug Delivery Systems. *Chemical Reviews* **119**, 6459-6506 (2019).
68. Jones, M.R., Seeman, N.C. & Mirkin, C.A. Programmable materials and the nature of the DNA bond. *Science* **347**, 1260901 (2015).
69. Cangialosi, A. et al. DNA sequence–directed shape change of photopatterned hydrogels via high-degree swelling. *Science* **357**, 1126-1130 (2017).
70. Pronk, S. et al. GROMACS 4.5: a high-throughput and highly parallel open source molecular simulation toolkit. *Bioinformatics* **29**, 845-854 (2013).
71. Abraham, M.J. et al. GROMACS: High performance molecular simulations through multi-level parallelism from laptops to supercomputers. *SoftwareX* **1**, 19-25 (2015).
72. Hanwell, M.D. et al. Avogadro: an advanced semantic chemical editor, visualization, and analysis platform. *Journal of cheminformatics* **4**, 1-17 (2012).
73. Sousa da Silva, A.W. & Vranken, W.F. ACPYPE-Antechamber python parser interface. *BMC research notes* **5**, 1-8 (2012).
74. Bayly, C.I., Cieplak, P., Cornell, W. & Kollman, P.A. A well-behaved electrostatic potential based method using charge restraints for deriving atomic charges: the RESP model. *The Journal of Physical Chemistry* **97**, 10269-10280 (1993).
75. Vanquelef, E. et al. RED Server: a web service for deriving RESP and ESP charges and building force field libraries for new molecules and molecular fragments. *Nucleic acids research* **39**, W511-W517 (2011).
76. Humphrey, W., Dalke, A. & Schulten, K. VMD: visual molecular dynamics. *J. Mol. Graphics* **14**, 33-38 (1996).
77. Jorgensen, W.L., Chandrasekhar, J., Madura, J.D., Impey, R.W. & Klein, M.L. Comparison of

simple potential functions for simulating liquid water. *The Journal of chemical physics* **79**, 926-935 (1983).

78. Joung, I.S. & Cheatham III, T.E. Determination of alkali and halide monovalent ion parameters for use in explicitly solvated biomolecular simulations. *The journal of physical chemistry B* **112**, 9020-9041 (2008).

79. Bussi, G., Donadio, D. & Parrinello, M. Canonical sampling through velocity rescaling. *The Journal of chemical physics* **126** (2007).

80. Parrinello, M. & Rahman, A. Polymorphic transitions in single crystals: A new molecular dynamics method. *Journal of Applied physics* **52**, 7182-7190 (1981).

81. Nosé, S. & Klein, M. Constant pressure molecular dynamics for molecular systems. *Molecular Physics* **50**, 1055-1076 (1983).

82. Darden, T., York, D. & Pedersen, L. Particle mesh Ewald: An N· log (N) method for Ewald sums in large systems. *The Journal of chemical physics* **98**, 10089-10092 (1993).

83. Essmann, U. et al. A smooth particle mesh Ewald method. *The Journal of chemical physics* **103**, 8577-8593 (1995).

84. Hess, B., Bekker, H., Berendsen, H.J. & Fraaije, J.G. LINCS: A linear constraint solver for molecular simulations. *Journal of computational chemistry* **18**, 1463-1472 (1997).

Methods

Materials. DNA and RNA oligonucleotide sequences were purchased from IDT and used without further purification, as listed in Supplementary Tables. Poly-L-lysine (PLL, 30-70 kDa, hydrobromide, P2636), Poly-D-lysine (30-70 kDa, hydrobromide, P7280), Poly-L-Arginine (70-150 kDa, hydrobromide, P1274), Polydiallyldimethylammonium chloride (PDDA, average M_w<100000, 522376), Polyethyleneimine (PEI , average M_w ~ 25000, 408727) and fluorescein isothiocyanate-labeled poly-L-lysine (FITC-PLL, 30-70 kDa, P3069) were purchased from Sigma-Aldrich, Inc. The averaged molecular weight of PLL is assumed to be 50 kDa, corresponding to an average of 240 lysine residues per chain.

Sample preparation. Stock solutions of DNA and RNA of 20 mM, and PLL of 100 mM total residue (or total charge) were prepared and stored under -20 °C. In the aqueous mixture, each lysine residue contributes one positive charge, and each DNA/RNA phosphate group contributes one negative charge. Hence, the negative and positive charge concentration in the mixture is defined as [e-]= [DNA phosphate]+[RNA phosphate] and [e+] = [PLL amine] =240×[PLL] respectively, where n is the number of nucleotides on a single DNA/RNA sequence, and [DNA], [RNA] and [PLL] denote the concentration of DNA, RNA and PLL in the mixture, respectively. Unless specified, [DNA phosphate] = [RNA phosphate]. In a typical experiment, an DNA/RNA solution with the target negative charge concentration containing 150 mM KCl and 40 mM Tris buffer (pH=7.5) was renatured by heating to 95 °C for 3 minutes using a PCR thermal cycler and then cooled down to room temperature, followed by incubation for 30 minutes. A PLL solution with the target positive charge concentration with KCl (150 mM) and 40 mM Tris buffer (pH=7.5) was separately prepared and then mixed thoroughly with the DNA/RNA solution using pipette. Salt concentration of KCl and NaCl in each experiment were adjusted according to the need.

Fluorescence imaging method. We performed imaging around 10 minutes after mixing the DNA/RNA solution and the PLL solution. Samples were introduced into customed chambers made with spacers. To inhibit the coacervate droplets settling down and then wetting the wall of the glass chamber, glass slides were first cleaned by ethanol and water to remove the contaminants, then immersed in the Pluronics F-127 solution (1 wt%) for around 1 hour and carefully rinsed using MilliQ water afterwards, followed by heated and dried inside the 65 °C oven for 1 hour. Bright field images of the coacervates were obtained on a Leica inverted microscope equipped with a 40X objective. Green fluorescence of FAM-labeled DNA and red fluorescence of Cy5-labelled RNA were activated with laser of the 488 nm and the 607 nm wavelength, respectively. The confocal images including Z-stacking were captured through a Spinning Disk confocal microscope (Zeiss) equipped with ×63 oil immersed lens (Plan-Apochromat). All images were representative of at least three independent tests and analyzed using the ImageJ software.

Fluorescence recovery after photobleaching (FRAP). FRAP experiments were

performed on a Carl Zeiss LSM 880 confocal microscope with a ×40 oil immersion objective. An area with radius of 0.5 μm was bleached with a 488-nm or 561-nm laser at 100% power; subsequent recovery of the bleached area was recorded with a 488-nm or 561-nm laser. Correction for photobleaching and normalization was performed via a custom code in Matlab. The final FRAP recovery data is the average of recovery curves collected from five independent measurements.

Flow cytometry. RNA-PLL droplets and DNA-PLL droplets were prepared with Cy5-RNA (2 μM) and FAM-DNA (2 μM), respectively. DNA-RNA-PLL multiphase droplets were stained with both Cy5-RNA and FAM-DNA. All samples were prepared at the charge concentration of [e+] = [e-] = 15 mM. Fluorescence intensity of 200 μL droplet sample were tested by the flow cytometer (BD FACSAriaIII) under the wavelength of 488/530 and 633/660. and the data wereanalyzed by FlowJo software (BD, USA).

Evaporation assay. A 0.5 μL sample containing DNA/RNA/PLL coacervates was pipetted onto a clean microscope glass slide under room conditions (Temperature = 25 °C, Humidity = 55–65%), forming an evaporating sessile droplet. ISOLAB GmbH microscope glass slides served as solid substrates for the droplets. To remove surface contaminants, the slides were first wiped with ethanol-moistened tissue, then sonicated in ethanol for 15 minutes, and finally rinsed with isopropyl alcohol and Milli-Q water. The cleaned slides were dried with nitrogen flow and placed in an oven at 65 °C for 1 hour. Fluorescence images of the evaporating droplets were captured using a Nikon Ti2-E Widefield microscope and processed with ImageJ (NIH) software.

CP-AFM measurements. Mechanical properties of DNA- and RNA-PLL droplets were characterized by an atomic force microscope (NanoWizard II, JPK). A spherical silica particle ($R \approx 4$ μm) was affixed to an AFM cantilever with a 0.1 N/m spring constant, following protocols described by Li and co-workers[44]. The spring constant was calibrated through a contact-based technique. AFM measurements were conducted by submerging the probe in a glass Petri dish containing 2 mL coacervate droplet suspensions. Prior to measurement, the probe and Petri dish underwent plasma treatment to eliminate contaminants and were rinsed with water to neutralize the surface. Droplet suspensions were prepared as previously mentioned, but with an extremely low concentration (0.6 mM total charge concentration, [e+] = [e-] = 0.3 mM) to improve laser signal gain. Freshly prepared droplet suspensions were always used, allowing for approximately 20 minutes of incubation to reach equilibrium. During a typical measurement, the probe made contact with the Petri dish's bottom at a constant velocity (1 μm/s) to establish zero-separation distance and initiate capillary condensation. The probe was held at zero-separation for 10 seconds to facilitate capillary bridge formation. Subsequently, the probe was raised at varying velocities between 0.2 μm/s and 2 μm/s, covering a 5 μm distance for each sample. For every retraction rate, twenty measurements were performed, and force-distance curves were monitored for both approach and retraction steps. Data analysis involved using JPK's data processing

941 software to correct the vertical tip position resulting from cantilever bending. The
942 cantilever deflection Δx was transformed into force using Hooke's law, $F = k\Delta x$, where
943 k represents the cantilever's spring constant.
944
945 **Temperature effects.** DNA/RNA/PLL droplets were prepared at room temperature and
946 introduced into a glass chamber situated on a transparent thermo plate (Tokai Hit Ltd.).
947 A TPi controller with feedback control via a temperature sensor established the desired
948 temperature. Following a 5-minute equilibration period, samples were observed with a
949 Leica inverted microscope. For heating droplets through light radiation, a similar
950 procedure was used, except the thermo plate was replaced by a light source (PHILIPS,
951 QVF135 MAX. 500 W).
952
953 **Circular dichroism (CD).** DNA and/or RNA oligos (5 μM) in Tris-HCl buffer
954 containing 25 mM Tris-HCl and 150 mM KCl/LiCl (pH 7.5) were heated at 95 °C for
955 3 min and cooled down at room temperature for 10 min. CD spectra were recorded on
956 a Jasco CD J-150 spectrometer with 1-cm path length quartz cuvette. Three scans from
957 220 nm to 340 nm at 1 nm intervals were accumulated and averaged.
958
959 **Droplet Microfluidics.** Microfluidic devices was prepared using a typical soft
960 lithography replica molding technology. First, a SU-8 photoresist (2025, MicroChem,
961 USA) mold with desired channel geometry was fabricated onto a silicon wafer using
962 maskless lithography (SF-100 Xcel, Intelligent Micro Patterning, LLC, USA). Then,
963 the pre-polymer base and curing agent of PDMS (Sylgard 184, Dow Corning, USA)
964 was mixed at a weight ratio of 10:1, degassed, and then poured onto the photoresist
965 mold and solidified at 65 ℃ overnight. Subsequently, the PDMS layer was detached
966 from the mold, and bonded to a glass substrate by oxygen plasma treatment. To fabricate
967 the electrodes, a low-melting-point metal wire (52225, Indium Incorporation, USA)
968 was inserted into the inlets of the designed channel near the expansion chamber and
969 then introduced into the whole channel under negative pressure applied to the outlets at
970 100 ℃. DNA/RNA and PLL droplets were generated using fluorinated oil (HFE7500,
971 3M, USA) supplemented with 2% (w/w) of surfactant (RAN Biotechnologies, USA) as
972 the continuous phase. The two batches of droplets were reinjected into the droplet
973 merging platform and separated by a gapping oil. An alternating current (AC) signal
974 with an amplitude of 750 Vp-p and a frequency of 30 kHz was applied to induce droplet
975 coalescence.
976
977 **Encapsulation of small molecules.** For partitioning experiments, 10 μL aliquots of a
978 DNA/RNA/PLL multiphase droplet of TERRA_M2 in the buffer containing 500 mM
979 KCl and 40 mM Tris (pH 7.5) were added to sample chambers on a cover glass slide,
980 with the charge concentration of [e-] = [e+] = 5 mM. Small quantities of the stock
981 solutions of the dye molecules were added to the multiphase droplets, mixed by gentle
982 pipetting, and visualized by excitation at the indicated wavelengths. DAPI (100 μM)
983 and dATP (50 μM) were excited at 380 nm. ThT (50 μM) and SYBI Green I (0.01 X
984 concentrate) were excited at 488 nm. NMM (10 uM), Nile Red (50 mg/mL), Rhodamine

B (100 μM) and Methylene Blue (100 μM) were excited at 561 nm.

Encapsulation of guest RNA. A mixture of 2 μM FAM-labeled rPU22 or rPU22_M2 guest molecules and DNA/RNA oligos of TERRA_M2 was prepared in a buffer containing 500 mM KCl and 40 mM Tris (pH 7.5), with a charge concentration of [e-] = [e+] = 5 mM. The mixture was renatured at 95 °C for 3 minutes, cooled to room temperature, and incubated for 30 minutes. PLL was then added to the mixture and mixed thoroughly using a pipette. The mixed samples were incubated at room temperature for 10 minutes before imaging with a Leica inverted microscope. The partition coefficient (K) was calculated from average fluorescence intensities using the formula $K = (I_{c,in} - I_b) / (I_{c,out} - I_b)$, where I_b, $I_{c,out}$, and $I_{c,in}$ represent the intensity of the dilute phase surrounding the multiphase droplets, the outer shell layer, and the inner core phase of the multiphase droplets, respectively. The Gibbs free energy change for partitioning was determined based on $\Delta G = -RT \ln K$.

Encapsulation of Broccoli RNA aptamer. A mixture containing 5 μM Broccoli RNA aptamer and/or 200 μM DFHBI-1T was first mixed with DNA/RNA oligos in a buffer containing 150 mM KCl, 40 mM Tris (pH 7.5), and 5 mM $MgCl_2$. To create multiphase droplets at 150 mM KCl, rPU22_M2 and d(S1-b-S2) were employed, maintaining a charge concentration of [e-] = [e+] = 2.5 mM. The mixture was renatured at 95 °C for 3 minutes, cooled to room temperature, and incubated for 30 minutes. PLL was then added to the mixture and mixed thoroughly using a pipette. The mixed samples were incubated at room temperature for 10 minutes before imaging with a Leica inverted microscope. The partition coefficient (K) was calculated from average fluorescence intensities using the formula $K = (I_{c,in} - I_b) / (I_{c,out} - I_b)$, where I_b, $I_{c,out}$, and $I_{c,in}$ represent the intensity of the dilute phase surrounding the multiphase droplets, the outer shell layer, and the inner core phase of the multiphase droplets, respectively. The Gibbs free energy change for partitioning was determined based on $\Delta G = -RT \ln K$.

Uptake of DNAzyme and substrate RNA. Guest molecules, including 5 μM Cy5-labeled DNAzyme, 2 μM FAM-labeled RNA substrate, RNA substrate 1, and RNA substrate 2, were individually incorporated into a buffer containing 40 mM Tris (pH 7.5), 10 mM MgCl2, and 150 mM KCl. The final sample volume was 10 μL. To create multiphase droplets at 150 mM KCl, rPU22_M2 and d(S1-b-S2) were utilized, maintaining a charge concentration of [e-] = [e+] = 2.5 mM. Samples were prepared by adding a PLL solution to the renatured nucleic acid buffer.

DNAzyme cleavage reaction. 10-23 DNAzyme (1 μM) in 25 mM Tris-HCl buffer containing 5 mM KCl and 5 mM $MgCl_2$ (pH=7.5) was heated at 95 ºC for 3 min and cooled down at room temperature for 10 min. Then DNAzyme were mixed with FAM-labeled RNA substrate (50 nM) that was partitioned into coacervates composed of PDDA (1 mM [e+]), rPU22_M2 and/or d(S1-b-S2) (1 mM [e-] in total). After incubating at 37 °C for 1 h, 1 M of NaCl was added to quench reactions and disrupt coacervates. Then the results were analyzed using 15% denaturing PAGE

(polyacrylamide gel) and scanned by FujiFilm FLA-9000 Gel Imager at 500 V. The data is fit to the exponential equation $y = A + Be^{-kt}$.

All-atom molecular dynamic (MD) simulations: All simulations were performed using the GROMACS 2021 package [70, 71] on the GPU nodes of HPC2021 at The university of Hong Kong. The chemical structures of small molecules (PSS, PVS, PLL, and ethanol) were built using the Avogadro software [72]. The force field parameters and topologies of small molecules were derived by the ACPYPE program [73] using amber2 for the "atom type" option. The partial charges of each molecule were fit based on the quantum mechanics calculation using the RESP program [74] on an online R.E.D. Server [75]. Data analysis and image export were performed using the VMD software [76].

For each simulation, 20 pairs of oppositely charged small molecules were solvated in a cubic water box with the size of 5.2×5.2×5.2 nm^3 and periodic boundary conditions. Then 20 Na^+ and 20 Cl^- ions were added to the systems. For simulations with ethanol, 700 ethanol molecules were inserted into the box to replace water molecules. The number ratio of ethanol to water molecules is around 1:3. The TIP3P water model was used [77]. The force field parameters for Na^+ and Cl^- ions were adapted from the reference [78]. The overall energy of the system was minimized using the steepest descent method followed by 500 ps NVT and 500 ps NPT equilibration simulations at 300 K and 1 bar. The equilibrated structure was used as the starting structure for MD simulation at 300 K and 1 bar. The simulation time step is 2 fs and the total simulation time is 500 ns. The V-rescale thermostat [79] was used for maintaining the temperature with a coupling time constant of 0.1 ps. The Parrinello-Rahman method [80, 81] was used to maintain the pressure at 1 bar with a coupling time constant of 2.0 ps. PME algorithm [82, 83] was applied to calculate the long-rang electrostatic interactions. The cutoffs of electrostatic potential and van der Waals potential were set to 1.2 nm. The LINCS algorithm was used to constrain all bonds with H-atoms [84]. MATLAB scripts were developed to analyze the radius distribution function $g(r)$ and calculate PMF as $-kTlog(g(r))$. Five independent simulations were performed for each condition with random initial positions.

Coarse-grained simulations: The coarse-grained simulations were performed using LaSSI simulation engine [69]. The PLL, RNA and DNA molecules were represented by sticker chains with the length of 20. The cubic simulation box with length of 200 contains 1000 PLL chains, 500 RNA chains, and 500 DNA chains. All molecules were randomly placed in the simulation box without overlap. Subsequently, a biasing potential was applied to all the beads to drive them toward the center of the simulation box. Next, an equilibrium process was performed for 1×10^8 Monte Carlo steps, during which the effective temperature was gradually reduced from 1000 to 1. Following equilibration, a production run of 2×10^{10} Monte Carlo steps were

performed. All stickers interacted via isotropic interactions. The homotypic interactions for PLL beads were set to 0.1 kT to capture the repulsive electrostatic interactions, while the heterotypic interactions for PLL-RNA and PLL-DNA were set to -0.28 kT and -0.20 kT, respectively. Homotypic interactions between RNA beads were 0. When the homotypic interactions between DNA beads were identical to those of RNA molecules, core-shell structures were observed. However, when the homotypic interactions between DNA were -0.1 kT, one-phase droplets formed. The relative moving frequencies of Monte Carlo moves are listed in the following table.

Move type	Relative frequency
Local	1000
Co-local	200
Multi-local	200
Snake	400
Chain translation	200
Small cluster translation	5
Cluster translation	1
Chain pivot	200
Double pivot	100

Data availability

The data that support this study are available within the paper and its Supplementary Information. Further details and raw images are also available from the corresponding authors upon reasonable request.

Code availability

All MATLAB codes used for fitting the FRAP data and analyzing the DNAzyme cleavage rate, in addition to codes utilized in the analysis of CP-AFM data, can be obtained from the corresponding authors upon request.

Acknowledgements

We are grateful to Prof. David A. Weitz and Prof. Julian A. Tanner for their continuous interests and insightful comments on this work. This work as supported by the General Research Fund (Nos. 17306221, 17317322, and 17306820) from the Research Grant Council (RGC) of Hong Kong, as well as the National Natural Science Foundation of China (NSFC)-RGC Joint Research Scheme (N_HKU718/19). H.C.S. was funded in part by the Croucher Senior Research Fellowship from Croucher Foundation and the Health@InnoHK program of the Innovation and Technology Commission of the Hong Kong SAR Government

Author contributions

W.G., Y.S. and H.C.S conceived and designed the project. W.G., X.L., A.B.K, Y.P., R.L., Y.W., K.K.L., T.M., F.W. and Z.Y. performed the experiments and analysed the data. F.C. and X.Z. performed molecular dynamic simulations. H.C.S supervised the study.

W.G., Y.S. X.Z. and H.C.S wrote the manuscript. All authors discussed the results and commented on the manuscript.

Competing interests

X.L. is a cofounder and director of Upgrade Biopolymers Limited, the work in this paper is not directly related to the work of the company. H.C. Shum is a scientific advisor of EN Technology Limited, MicroDiagnostics Limited, and PharmaEase Technology Limited in which he owns some equity, and a managing director of the research centre, namely Advanced Biomedical Instrumentation Centre Limited. The works in the paper is, however, not directly related to the works of these entities, as far as we know.